

This is an Open Access document downloaded from ORCA, Cardiff University's institutional repository: <https://orca.cardiff.ac.uk/id/eprint/117739/>

This is the author's version of a work that was submitted to / accepted for publication.

Citation for final published version:

Farrell, Alan C., Meng, Xiao, Ren, Dingkun, Kim, Hyunseok, Senanayake, Pradeep, Hsieh, Nick Y., Rong, Zixuan, Chang, Ting-Yuan, Azizur-Rahman, Khalifa and Huffaker, Diana L. 2019. InGaAs-GaAs nanowire avalanche photodiodes toward single-photon detection in free-running mode. Nano Letters 19 (1) , pp. 582-590. 10.1021/acs.nanolett.8b04643

Publishers page: <http://dx.doi.org/10.1021/acs.nanolett.8b04643>

Please note:

Changes made as a result of publishing processes such as copy-editing, formatting and page numbers may not be reflected in this version. For the definitive version of this publication, please refer to the published source. You are advised to consult the publisher's version if you wish to cite this paper.

This version is being made available in accordance with publisher policies. See <http://orca.cf.ac.uk/policies.html> for usage policies. Copyright and moral rights for publications made available in ORCA are retained by the copyright holders.



InGaAs-GaAs Nanowire Avalanche Photodiodes Toward Single Photon Detection in Free-Running Mode

Alan C. Farrell,^{§,†} Xiao Meng,^{§,‡} Dingkun Ren,^{§,†} Hyunseok Kim,^{,†} Pradeep Senanayake,[†] Nick
Y. Hsieh,[†] Zixuan Rong,[†] Ting-Yuan Chang,[†] Khalifa M. Azizur-Rahman,[‡] and Diana L.
Huffaker^{†,‡,§}*

[†]Department of Electrical Engineering, University of California, Los Angeles, Los Angeles,
California 90095, USA

[‡]School of Physics and Astronomy, Cardiff University, Cardiff, Wales CF24 3AA, UK

[§]California NanoSystems Institute, University of California at Los Angeles, Los Angeles,
California 90095, USA

KEYWORDS: nanowires, InGaAs-GaAs, single photon detection, avalanche photodiodes, near-
infrared, free-running mode

ABSTRACT

Single photon detection at near-infrared (NIR) wavelengths is critical for light detection and ranging (LiDAR) systems used in imaging technologies such as autonomous vehicle trackers and atmospheric remote sensing. Portable, high-performance LiDAR relies on silicon-based single-photon avalanche diodes (SPADs) due to their extremely low dark count rate (DCR) and afterpulsing probability, but their operation wavelengths are typically limited up to 905 nm. Although InGaAs-InP SPADs offer an alternative platform to extend the operation wavelengths to eye-safe ranges, their high DCR and afterpulsing severely limit their commercial applications. Here we propose a new selective absorption and multiplication avalanche photodiode (SAM-APD) platform composed of vertical InGaAs-GaAs nanowire arrays for single photon detection. Among a total of 4400 nanowires constituting one photodiode, each avalanche event is confined in a single nanowire, which means that the avalanche volume and the number of filled traps can be drastically reduced in our approach. This leads to an extremely small afterpulsing probability compared with conventional InGaAs-based SPADs and enables operation in free-running mode. We show DCR below 10 Hz, due to reduced fill factor, with photon count rates of 7.8 MHz and timing jitter less than 113 ps, which suggest that nanowire-based NIR focal plane arrays for single photon detection can be designed without active quenching circuitry that severely restricts pixel density and portability in NIR commercial SPADs. Therefore, the proposed work based on vertical nanowires provides a new degree of freedom in designing avalanche photodetectors and could be a stepping stone for high-performance InGaAs SPADs.

Avalanche photodetectors (APDs) have become the technology of choice for the most demanding photon detection applications, including time-resolved photoluminescence,¹ laser rangefinders,² time-of-flight 3D scanners,³ and light detection and ranging (LiDAR).⁴ More recently, demand for high volume, low-cost LiDAR has seen a dramatic rise with the development of imaging technologies for autonomous vehicles and three-dimensional (3D) mobile mapping systems.^{5,6} Silicon-based single photon avalanche diodes (SPADs) are widely used in many applications due to their excellent performances including the capability to operate in free-running mode, extremely low dark count rate (DCR), high photon detection efficiency (PDE), and low timing jitter. However, in certain instances, *e.g.*, quantum key distribution and eye-safe LiDAR,^{7,8} it is advantageous to be able to detect light in the near-infrared (NIR) regime over 1 μm , where silicon SPADs fail to offer acceptable PDE (less than 5% over 1 μm).⁹ Alternatively, commercially available InGaAs-InP separate absorption-multiplication (SAM) APDs with longer cutoff wavelengths, tested in Geiger mode (*i.e.* above the breakdown voltage),¹⁰⁻¹² have very high DCR. InGaAs-InP SPADs were further specifically designed for single photon detection that takes into account the much higher electric fields present in the avalanche region of a SPAD to reduce trap-assisted tunneling responsible for the high DCR.^{13,14} Although considerable progress has been made towards improving performance—it is now common to achieve 10-20 % PDE with a DCR of a few kHz (14,15)—there still exists a fundamental limit to the maximum count rate.^{15,16}

As opposed to linear mode APDs, the count rate in a SPAD is not limited by avalanche build-up time, but rather by afterpulsing effect, which is caused by the detrapping of carriers from local trap states that have been filled during avalanche events. Since the detrapped carriers induce new avalanche events (afterpulsing), decreasing the defect density in material is crucial for reducing afterpulsing probability. However, the task of reducing the defect density in III-V semiconductors

down to levels comparable to silicon remains a significant challenge. As a result, other techniques have been employed to mitigate the effects of afterpulsing. The most commonly used approach to reducing afterpulsing is to actively quench the SPAD by reducing the bias below the breakdown voltage for a certain time span (dead time) after each avalanche event. However, photons cannot be detected during the dead time and this limits the photon counting rate to about 100 kHz. Another active quenching technique is to limit the current flow through the SPAD to reduce the number of traps filled by an avalanche event. This can be achieved by using ultra-short gated bias (*e.g.* overbiasing the SPAD for a period of less than 1 ns). However, the requirement for sophisticated electronics for cancelling large transient pulses limits its usefulness in applications requiring compact SPAD arrays (*e.g.* 3D imaging using SPAD array).^{17,18} In addition, such fast gating approach requires precise synchronization between the light source and gated bias to maximize the detection efficiency, which makes it unsuitable for applications with unknown photon arrival times (*e.g.* LiDAR and time-resolved fluorescence spectroscopy) where free-running operation is needed.

In this work, we present a vertical nanowire array SAM-APD operating in Geiger mode. Our proposed approach reduces afterpulsing by confining the volume of semiconductor material exposed to the high current flow of an avalanche event within one nanowire. Bottom-up integrated vertical nanowires with an InGaAs absorption layer and GaAs avalanche layer comprise the active area of the APD, where the low fill factor suppresses the total number of traps, resulting in improved DCR. Although various types of nanowire APDs have been investigated in recent studies,¹⁹⁻²⁷ there are no reports on nanowire APDs operating above their breakdown voltages (*i.e.*, Geiger mode-APD or SPAD) for NIR photon detection, to the best of our knowledge. Here, we demonstrate operation of InGaAs-GaAs nanowire-based SAM-APDs in Geiger mode at 1064 nm. We show that the dark current at 95% of the breakdown voltage is below the noise floor of the

measurement setup, indicating a remarkably low dark current within a single nanowire. Given that the ratio of the volume of a single nanowire to a bulk SPAD of equal effective volume is extremely small, a dramatic reduction in afterpulsing probability is expected. Additionally, we show a measured DCR below 10 Hz with photon count rates approaching 8 MHz in free running mode and timing jitter less than 113 ps at 77 K. Our work paves the way toward realizing nanowire-based NIR SPADs operating in free-running mode with high photon count rates.

Growth of nanowire SAM-APDs. Although axial heterostructure formation in nanowires is routinely achieved with a variety of materials using catalyzed growth techniques, it remains a challenge for catalyst-free nanowire epitaxy. Several examples of core-shell InGaAs-GaAs heteroepitaxy exist in the literature,²⁸⁻³⁰ but reports on axial heteroepitaxy are limited to quantum dot formation,³¹ low indium composition,³² or thin InGaAs layers.³³ The nanowire SAM-APD design for single photon detection requires thicker InGaAs axial layer to enhance the absorption, and thus a different approach is necessary. The commonly used gallium precursor, trimethylgallium, was replaced with triethylgallium to enhance the growth rate in the vertical direction for selective-area epitaxy with large-area openings.^{34,35} A schematic diagram of nanowire SAM-APDs based on axial InGaAs-GaAs heterostructures is shown in Figure 1a. Since any overgrowth in the lateral directions can form a shunt path for photocarriers through the spacing between segments (or multiplication regions)³⁶ and results in non-uniformity of internal gain, we have developed purely axial growth of InGaAs on top of GaAs nanowires. A 100 nm-long zinc-doped InGaAs layer was introduced as a contact layer, and an undoped InGaP shell was used for surface passivation. Details of the nanowire growth procedures can be found in the Methods section.

The size of nanowire array is $40\text{ }\mu\text{m} \times 40\text{ }\mu\text{m}$, containing ~ 4400 nanowires (where nanowire pitch is 600 nm) per device. Device layer thicknesses were calibrated by measuring the height of the nanowires after the addition of each layer using scanning electron microscopy (SEM), as shown in Figure 1b. No increase in nanowire diameters, within measurement error of the SEM (~ 3 nm), was observed from the first GaAs layer to the final InGaAs layer. The indium composition of InGaAs segment is $\sim 26\%$, which is confirmed by energy dispersive X-ray spectroscopy (EDX) and photoluminescence measurements (Supporting Figure S1). Device fabrication was accomplished using standard photolithography (described in detail in the Methods section) similar to standard planar device processing (Figure 1c). The active area of the nanowire SAM-APDs is square shaped, reflecting the square nanowire array layout. Figure 1d shows a close-up view of the active area where the partially exposed nanowires with self-assembled plasmonic gratings are clearly visible, allowing light absorption through top illumination.^{26,27}

Dark count rate and photon count rate. Current-voltage (I-V) characteristics were measured under vacuum at various temperatures. Figure 1e shows the result of several repeated measurements on one device at 77 K. The variation of the breakdown voltage from one measurement to the next is immediately apparent. Two features of this behavior are important to note: (1) the breakdown voltage is varying randomly (*i.e.*, it is not monotonically increasing or decreasing), and (2) the electrical characteristics of the nanowire SAM-APDs are not degrading, which has been observed after avalanche breakdown of nanowire APDs.²⁴ The random variation in the breakdown voltage is a direct result of the extremely low dark current at the breakdown voltage. The dark current is below the noise floor of the measurement equipment below 200 K as shown in Figure 1f. Although the dark current is below the noise floor of the measurement equipment at 77 K, from the temperature dependence of the dark current we estimate a dark current

of 1 fA or lower at breakdown. During the voltage sweep, this means that less than 7 electrons flow through the device with 4400 nanowires during each voltage step lasting 1 ms. Of these less than 7 electrons, the majority are expected to originate from the surface of the nanowire—due to the very high surface-to-volume ratio—and do not initiate breakdown.³⁷ Therefore, it is very likely that the random fluctuation of breakdown voltage is due to the probability for dark carriers to initiate breakdown during a given voltage step being less than one during the voltage sweep measurement. This effect has been reported in extremely small volume silicon APDs as well.³⁸ It should also be noted that each avalanche event is confined in a single nanowire among a total of 4400 nanowires, while these nanowires will not have perfectly identical breakdown voltages. Therefore, avalanche voltage will be also affected by the specific nanowire that is triggering the breakdown process, and this will cause additional fluctuation in the breakdown voltage. It is also worth mentioning that the fabricated devices show highly uniform electrical characteristics, indicating the reliability of nanowire epitaxy and fabrication processes (Supporting Figure S2).

The nanowire SAM-APDs are passively quenched with a 1 M Ω resistor and operated in free-running mode, *i.e.*, no gating or dead time is used, as shown in Figure 2a (described in detail in the Methods section). This is the simplest and most desirable configuration for photon counting as no active quenching electronics are required and photons can be detected as they arrive, rather than only during gated periods. Figure 2b shows the pulse shapes at different applied biases for dark carrier-initiated avalanche events at 77 K. Both the pulse amplitude and the pulse width increase with the applied bias. The increase in pulse width is due to a sustained avalanche caused by the high electric field,³⁹ but does not negatively affect SPAD performance except for a slight decrease in the maximum count rate. A real-time sweep of the device at a reverse bias of 29 V at 77 K is shown in Figure 3a. A total of 28 pulses were measured during the entire 10 second sweep,

corresponding to a DCR of 2.8 Hz in free-running mode. To place this in context, we note that commercial InGaAs-InP SPADs typically achieve a DCR of 1-2 kHz at this temperature in gated mode, as opposed to the free-running mode used in this work. Next, real-time sweep was measured with a continuous-wave (CW) 1064 nm incident light source on the nanowire SAM-APDs, as shown in Figure 3b. A total of 31 photon-initiated pulses were measured during a 4 μ s sweep, corresponding to a photon count rate of 7.8 MHz. Close examination of the pulse separation, shown in Figure 3c, reveals that photons can be detected at a minimum of 40 ns apart, corresponding to a maximum photon count rate of 25 MHz. This is in stark contrast to commercial InGaAs-InP SPADs, which are limited to counting rates up to 100 kHz as a direct result of the dead time necessary to suppress afterpulsing.

The DCR is usually presented as a function of the overbias, *i.e.*, the bias above the breakdown voltage. However, in this case it is difficult to determine the breakdown voltage at 77 K due to the randomness of the breakdown voltage after successive DC sweeps. We take the lowest voltage at which breakdown occurs, 17 V, as the breakdown voltage at 77 K. At 200 K, the generation current increases and as a result the breakdown voltage variation is much smaller. The temperature coefficient of breakdown is estimated to be 8.1 mV/K, which is comparable to values reported for planar GaAs.⁴⁰ Figure 4 shows the DCR from 77 – 125 K as a function of overbias, V_{OB} . There is no clear temperature dependence in this temperature range, indicating that the source of the dark current is likely due to trap-assisted tunneling. The DCR is expected to be more temperature-dependent at higher temperatures due to more dark carriers from SRH generation-recombination process and minority carrier diffusion. The low DCR is mainly due to the small active region of our nanowire devices. In other words, the total population of trap states and dark carriers is much smaller than that of other planar SPADs. We also note that an overbias of ~ 10 V

used in our measurements is relatively high, while this is also technically possible in conventional InGaAs(P)-based SPADs.⁴¹ More importantly, the operating range of SPADs is determined by the structural designs, and in our designs, the thickness of GaAs multiplication regions is 400 nm, which is much thinner than conventional counterparts. As a result, a higher overbias is required to increase avalanche probability in our devices. Nevertheless, our device has sustained an overbias of 10 V or higher for at least 10 seconds.

Afterpulsing probability. The effect of afterpulsing can be observed by measuring the dependence of the DCR on the dead time. The simplest approach to reset a self-sustaining avalanche process is to passively quench the avalanche using a resistor in series with the SPAD. When large current flows through the resistor, the increased potential drop across the resistor reduces the potential across the SPAD below the breakdown voltage and terminates the avalanche event. The trapped carriers are then released at a rate determined by the detrapping lifetime.

Since we operate our nanowire SAM-APDs in free-running mode, there is no active quenching and no means to control the dead time. However, afterpulsing occurs within the first few microseconds of a dark pulse. Therefore, by looking at the time spacing between pulses in free-running mode, we can determine whether a pulse was caused by a standard Shockley-Read-Hall process, or by carrier detrapping (afterpulsing). For this, we first assume that if two pulses are less than 100 μ s apart, then the second pulse is assumed to be an afterpulse. Since the average time between dark pulses is greater than 50 ms, it is highly unlikely that two uncorrelated pulses will be found within 100 μ s apart from each other. Conversely, we also assume that if two pulses are greater than 100 μ s apart, then the second pulse is not correlated to the first pulse. To verify the validity of this second assumption, we have measured fifty dark pulses at 77 K for each applied bias and found secondary pulses only up to 2 μ s, but not from 2 μ s up to 100 μ s (Supporting Figure

S3). Since detrapping of carriers is a spontaneous process, it is reasonable to assume that there will be no afterpulsing after 100 μs , given that afterpulsing is observed only from 0 μs to 2 μs and not from 2 μs to 100 μs .

Based on this assumption, we have measured the afterpulsing probability. Within a 2 μs time window secondary pulses are observed as V_{OB} is increased, as shown in Figure 5a, where the primary pulse is located at $t = 0$. At $V_{\text{OB}} = 9 \text{ V}$, there are zero secondary pulses out of fifty measured primary pulses; at $V_{\text{OB}} = 10 \text{ V}$, there is one secondary pulse; at $V_{\text{OB}} = 11 \text{ V}$, there are five secondary pulses; and, at $V_{\text{OB}} = 12 \text{ V}$, there are 15 secondary pulses. Using simple frequentist statistics, we estimate the afterpulsing probability, p , by

$$p = \frac{N}{N + 50} \quad (1)$$

where N is the number of secondary pulses (Figure 5b). Note that a secondary pulse can cause its own afterpulse, and so this must be counted as a new primary pulse and added to the fifty original primary pulses in the denominator. Two important conclusions are drawn from these data: (1) the afterpulsing probability is significantly lower than bulk SPADs operating in free running mode, where the afterpulsing probability is unity,⁴² and (2) even at the highest applied bias, the afterpulsing terminates after only 1.5 μs . Furthermore, as the temperature is increased, the detrapping lifetime decreases,⁸ thus the afterpulsing will terminate at an even shorter time span. This opens the possibility of using sub-microsecond dead-times in an actively quenched operating mode, allowing megahertz count rates with a nearly zero afterpulsing probability (at the expense of increased circuit complexity).

Timing Jitter. The timing jitter of a SPAD is an important performance metric, especially for timing applications such as LiDAR. The measured timing jitter is a convolution of the timing jitter of each individual element in the measurement setup (described in detail in the Methods section).

Assuming that the SAM-APD, laser, oscilloscope, and amplifier have Gaussian timing distributions, the total timing jitter can be expressed as follows

$$\tau^2 = \tau_{APD}^2 + \tau_{laser}^2 + \tau_{osc}^2 + \tau_{amp}^2 \quad (2)$$

The total timing jitter is measured, and the timing jitter of the oscilloscope is acquired from the equipment specifications. However, the remaining terms in Eq. (2) are unknown. Therefore, we first replace the SAM-APD with a pulsed voltage source with a known timing jitter ($\tau_{pulse} = 50$ ps, from equipment specifications) such that

$$\tau^2 = \tau_{pulse}^2 + \tau_{osc}^2 + \tau_{amp}^2 \quad (3)$$

Figure 5c shows the timing distribution measurements in each case. Using a pulsed voltage source, a total timing jitter of 283 ps is measured at 77 K. Since $\tau_{pulse} = 20$ ps and $\tau_{osc} = 50$ ps, we find $\tau_{amp} = 278$ ps. Replacing the pulsed voltage source with the nanowire SAM-APD illuminated by the pulsed laser, we measure a timing jitter of 285 ps, from which we estimate $\tau_{APD}^2 + \tau_{laser}^2 = 39$ ps. Since the timing jitter of the laser is non-zero (the exact value is unknown), we conclude that τ_{APD} is less than 39 ps. We should note that because τ_{amp} is large compared to the rest of the components, its estimated value should not be considered precise. If we assume 10 ps error in the full-width at half-maximum (FWHM) of the measured data with a pulsed voltage source (*i.e.* 283 ± 10 ps) and a laser (*i.e.* 285 ± 10 ps), then τ_{APD} could be as large as 113 ps.

Toward high-performance SPADs. The purpose of this work is to show that the nanowire platform can provide certain performance improvements for single photon detection, namely a reduction in DCR and afterpulsing probability. The reduction in DCR is accomplished through a reduction of the fill factor to reduce the bulk volume and the number of traps. To prove this concept, we studied the device performance at the technologically relevant wavelength of 1064

nm. The reduction in afterpulsing probability is accomplished by confining the avalanche current to the volume of a single nanowire, limiting the number of traps filled by the large current flow. We show both extremely low DCR < 10 Hz and significantly reduced afterpulsing for a range of applied biases. The lack of any significant afterpulsing allows operation in free-running mode, which eliminates the dead time limiting counting rates in commercial InGaAs-InP SPADs. We have measured a photon count rate of nearly 8 MHz and estimated the maximum count rate to be 25 MHz based on pulse separation. Despite the impressive performance, there are several challenges that must be addressed to make this a viable commercial technology. First, although the photon detection efficiency (PDE) is not measured, it is likely very low compared to commercial technology. This is because the plasmonic grating antenna is not optimized to maximize the optical absorption at 1064 nm (Supporting Figure S4 and S5). Fortunately, it is a simple matter to address, as the absorption can be increased to $> 40\%$ at 1064 nm by modifying the geometry of nanowires and the metal grating.^{43,44} The optimized peak responsivity of those detectors yields 0.28 A/W at 1100 nm. Although this is less than that of a planar InGaAs detector (~ 0.7 A/W), we note that the signal-to-noise ratio (SNR) of a SPAD is proportional to $\text{PDE}/(\text{DCR})^{1/2}$, and thus a large improvement in SNR is still expected due to the extremely low DCR in nanowire detectors. It is also worth mentioning that the absorption efficiency could be further improved by forming vertical nanowire-based photonic crystals, which have been already demonstrated as an effective approach to design efficient nanowire-based absorbers.^{45,46} The second critical issue that must be addressed is the maximum operating temperature, which is 150 K for the nanowire SAM-APDs in this work. Above this temperature the devices quickly degrade after several measurements (Supporting Figure S6). This is likely due to an increase in the current flow originating from the surface of the nanowires. Although the nanowires are passivated with

InGaP shell, the depletion region extends past the top surface of the BCB spacer and is exposed to air, leading to an increase in surface leakage current. We show in a previous study of GaAs nanowire photodiodes that the depletion region needs to be entirely confined beneath the BCB to achieve the best detector performance.⁴⁷ A possible solution is to apply a second layer of BCB after device fabrication to passivate the exposed portion of the nanowires, or chemical passivation with ammonium sulfide followed by encapsulation with SiO₂.⁴⁸

In summary, we have demonstrated a nanowire-based InGaAs-GaAs SAM-APD platform for single photon detection at 1064 nm. The growth of nanowire heterostructures was carefully calibrated to achieve purely axial integration of absorption and multiplication layers to prevent the formation of shunt paths. The nanowire SAM-APDs were passively quenched and operated in free-running mode, giving a photon count rate of 7.8 MHz, which is almost two orders of magnitude higher than that of commercial InGaAs-InP SPADs operating in free-running mode. The enabling physics lies in the mitigation of afterpulsing effect; the avalanche volume and number of traps were minimized in the proposed device, where each avalanche event was confined within a single nanowire. It was also shown at 77 K that the DCR was below 10 Hz and the afterpulsing probability was less than 0.25 at an overbias of 12 V, while the timing jitter was less than 113 ps. Our work provides a foundation for highly efficient single photon detection at NIR or even longer wavelengths.

METHODS

Sample preparation. n^+ -GaAs (111)B wafers (Wafertech) were removed from sealed packaging and immediately transferred into an e-beam evaporator and 20 nm SiO₂ was deposited at a rate of 1 Å/s at 1 μTorr pressure. Wafers were patterned using e-beam lithography with 80 nm diameter holes with a 600 nm pitch covering an area of 40 μm × 40 μm for each pixel. After developing the e-beam resist, the SiO₂ mask was etched in an Oxford 80 Plus reactive ion etcher (RIE) at a rate of 40 nm/min for 1 min to expose the substrate in the patterned areas using CF₄ and O₂ chemistry. Wafers were then spin-coated with AZ5214 photoresist without removing the e-beam resist and diced into 1 cm × 1 cm pieces. The pieces were then cleaned by first rinsing with acetone to remove the AZ5214, then placed in a heated NMP at 60 °C and ultrasonicated for 5 hours to remove the e-beam resist. After rinsing with IPA, the pieces underwent a final cleaning by oxygen plasma using a Matrix downstream asher for 6 min at 240 °C.

Nanowire Growth. Nanowires were grown on n-doped GaAs (111)B substrate by catalyst-free selective-area epitaxy using metal-organic chemical vapor deposition (MOCVD) in an Emcore vertical-flow reactor at a pressure of 60 torr. Source materials for In, Ga, As, P, and Zn were trimethylindium (TMIn), triethylgallium (TEGa), tertiarybutylarsine (TBAs), tertiarybutylphosphine (TBP), and diethylzinc (DEZn), respectively. Before loading the sample, native oxide was etched in a HF:H₂O (1:200) solution for 45 seconds, rinsed with deionized water, dried with N₂, then immediately transferred to the MOCVD reactor. The temperature was ramped to 680 °C and held for 10 minutes under TBAs overpressure to remove native oxide from the substrate surface. A 400 nm nominally undoped GaAs avalanche layer was grown for 20 minutes at 680 °C with V/III ratio of 40. A 300 nm p -GaAs layer was grown for 9 minutes with [DEZn]/[TEGa] = 0.1. A 400 nm nominally undoped InGaAs absorption layer was grown for 8

minutes with $[\text{TMIn}]/([\text{TMIn}]+[\text{TEGa}]) = 0.4$. A 100 nm *p*-InGaAs contact layer was grown for 2 minutes with $[\text{DEZn}]/([\text{TMIn}]+[\text{TEGa}]) = 0.5$. The temperature was ramped down to 590 °C under TBAs overpressure and stabilized for 2 minutes. Then, TBAs was shut off and the growth chamber was cleared under H₂ for 15 seconds, followed by TBP flow for 15 seconds. Finally, a nominally undoped 15 nm InGaP shell was grown for 2 minutes with $[\text{TMIn}]/([\text{TMIn}]+[\text{TEGa}]) = 0.4$. After the growth, the temperature was ramped down under TBP overpressure. The final nanowire diameter and height were 150 nm and 1.2 μm, respectively.

Device fabrication. Samples were soaked in buffered oxide etchant (6:1 BOE) for 30 seconds to remove the SiO₂ mask. After rinsing, they were dried on a hotplate at 180 °C for 2 minutes. Samples were spin-coated with photosensitive Cyclotene 4000 Series BCB (Dow Chemical) and patterned with vias for contact to the substrate using photolithography. After curing at 250 °C for 1 hour, residual BCB was removed by RIE for 1 minute at a rate of 80 nm/min. Ohmic contact to the substrate was achieved with Ge/Ni/Ge/Au metallization, followed by annealing at 380 °C for 30 sec. Following the lift-off, the top 210 nm of the nanowires were exposed by RIE. Contacts to the nanowires were defined using photolithography, and Au/Zn/Au was deposited with the samples mounted at a 45° angle to allow partial exposure of the nanowires. Following the lift-off, the samples were annealed at 340 °C for 30 sec.

Dark and photon counts. The nanowire SAM-APD sample was placed in a cryogenic chamber (LakeShore TTPX) to carry out low temperature measurements. DC bias voltage was applied to the device through a 1 MΩ quenching resistor using an Agilent B2961A source measurement unit (SMU). When the devices were overbiased, avalanche current pulses were converted into voltage pulses by a 50 Ω terminator which were then amplified by two cascaded radio frequency (RF) amplifiers. Each amplifier had a bandwidth of 2 GHz and gain of 25 dB. Amplified avalanche

pulses were discriminated and counted by a time-correlated single photon counter (PicoHarp 300). A 20 GHz digital oscilloscope (Tektronix DSA 72004C) was used to monitor the avalanche pulses. This deep memory oscilloscope was able to capture signal data with 4 ns resolution over a time window as long as 200 ms, so the dark and photon count rates were calculated by analyzing recorded signal data. The photon source for the photon counts measurements was a fiber-coupled 1064 nm CW laser (Orbits Lightwave Eternal SlowLight). The CW laser light was attenuated by a HP 8156A variable optical attenuator (VOA) before illuminating the devices. During the photon counts measurement, the laser power was slowly increased until the counts rate was saturated (i.e. reaching the maximum photon count rate).

Timing jitter. For timing jitter measurements, the biasing circuit remained the same as the dark and photon counts measurement, but the CW laser was replaced with a pulsed laser (NKT SuperK EXTREME EXW-12) operating at 1064 nm and a repetition frequency of 1.95 MHz. NIM output signal from the laser and the avalanche pulses from the device were connected to the channels of PicoHarp 300. The histogram of time correlation between the two channels were plotted by the PicoHarp software. The bin resolution of the histogram was 4 ps. In the case of using a pulsed voltage source, an HP 8116A Pulse Generator was used. The generated square pulses (with pulse width of 20 ns) were used to simulate the avalanche pulses from the nanowire SAM-APDs.

ASSOCIATED CONTENTS

Supporting Information

The Supporting Information is available free of charge on the ACS Publications website.

(Material properties of nanowires, device uniformity, afterpulsing, absorption efficiency of nanowire SAM-APDs, and device failure at 200 K)

AUTHOR INFORMATION

Author contributions

§A.C.Farrell, X.Meng, and D.Ren contributed equally to this work.

Corresponding Author

*Email: hyunseokkim@ucla.edu

ORCID

Alan C. Farrell: 0000-0001-6083-9121

Xiao Meng: 0000-0002-7061-9840

Dingkun Ren: 0000-0001-9470-1956

Hyunseok Kim: 0000-0003-3091-8413

Notes

The authors claim no competing financial interests.

ACKNOWLEDGEMENTS

We acknowledge the following user facilities – UCLA Nanoelectronics Research Facility as well as Integrated Systems Nanofabrication Cleanroom (ISNC) and Electron Imaging Center for NanoMachines (EICN) in California NanoSystems Institute (CNSI). The authors acknowledge the generous financial support of this research by Air Force Office of Scientific Research (FA9550-15-1-0324), Defense Advanced Research Projects Agency (W911NF-13-1-0188), National Science Foundation (grant no. ECCS-1509801 and ECCS-1711967), Institute for Information & communications Technology Promotion (IITP) grant funded by the Korea government (MSIT) (No.20170000740011001, A Generic Technology Study for Quantum Photonic Integrated Circuits) and Sêr Cymru grants in Advanced Engineering and Materials.

REFERENCES

1. Gorgis, A.; Flissikowski, T.; Brandt, O.; Chèze, C.; Geelhaar, L.; Riechert, H.; Grahn, H., Time-resolved photoluminescence spectroscopy of individual GaN nanowires. *Physical review B* **2012**, 86 (4), 041302.
2. Niclass, C.; Soga, M.; Kato, S. In *A 0.18 μm CMOS single-photon sensor for coaxial laser rangefinders*, 2010 IEEE Asian Solid State Circuits Conference (A-SSCC), 2010; 4-1.
3. Lussana, R.; Villa, F.; Dalla Mora, A.; Contini, D.; Tosi, A.; Zappa, F., Enhanced single-photon time-of-flight 3D ranging. *Optics express* **2015**, 23 (19), 24962-24973.
4. Gatt, P.; Johnson, S.; Nichols, T., Geiger-mode avalanche photodiode lidar receiver performance characteristics and detection statistics. *Applied optics* **2009**, 48 (17), 3261-3276.
5. Schwarz, B., LIDAR: Mapping the world in 3D. *Nature Photonics* **2010**, 4 (7), 429.
6. Ackerman, E., Lidar that will make self-driving cars affordable. *IEEE Spectrum* **2016**, 53 (10), 14-14.
7. Stucki, D.; Ribordy, G.; Stefanov, A.; Zbinden, H.; Rarity, J. G.; Wall, T., Photon counting for quantum key distribution with Peltier cooled InGaAs/InP APDs. *Journal of Modern Optics* **2001**, 48 (13), 1967-1981.
8. McCarthy, A.; Ren, X.; Della Frera, A.; Gemmell, N. R.; Krichel, N. J.; Scarcella, C.; Ruggeri, A.; Tosi, A.; Buller, G. S., Kilometer-range depth imaging at 1550 nm wavelength using an InGaAs/InP single-photon avalanche diode detector. *Optics express* **2013**, 21 (19), 22098-22113.
9. Buller, G.; Collins, R., Single-photon generation and detection. *Measurement Science and Technology* **2009**, 21 (1), 012002.

10. Lacaita, A.; Zappa, F.; Cova, S.; Lovati, P., Single-photon detection beyond 1 μm : performance of commercially available InGaAs/InP detectors. *Applied Optics* **1996**, 35 (16), 2986-2996.
11. Ribordy, G.; Gisin, N.; Guinnard, O.; Stuck, D.; Wegmuller, M.; Zbinden, H., Photon counting at telecom wavelengths with commercial InGaAs/InP avalanche photodiodes: current performance. *Journal of Modern Optics* **2004**, 51 (9-10), 1381-1398.
12. Hiskett, P. A.; Buller, G. S.; Loudon, A. Y.; Smith, J. M.; Gontijo, I.; Walker, A. C.; Townsend, P. D.; Robertson, M. J., Performance and design of InGaAs/InP photodiodes for single-photon counting at 1.55 μm . *Applied Optics* **2000**, 39 (36), 6818-6829.
13. Verghese, S.; Donnelly, J. P.; Duerr, E. K.; McIntosh, K. A.; Chapman, D. C.; Vineis, C. J.; Smith, G. M.; Funk, J. E.; Jensen, K. E.; Hopman, P. I., Arrays of InP-based avalanche photodiodes for photon counting. *IEEE Journal of Selected Topics in Quantum Electronics* **2007**, 13 (4), 870-886.
14. Itzler, M. A.; Ben-Michael, R.; Hsu, C.-F.; Slomkowski, K.; Tosi, A.; Cova, S.; Zappa, F.; Ispasoiu, R., Single photon avalanche diodes (SPADs) for 1.5 μm photon counting applications. *Journal of Modern Optics* **2007**, 54 (2-3), 283-304.
15. Itzler, M. A.; Jiang, X.; Entwistle, M.; Slomkowski, K.; Tosi, A.; Acerbi, F.; Zappa, F.; Cova, S., Advances in InGaAsP-based avalanche diode single photon detectors. *Journal of Modern Optics* **2011**, 58 (3-4), 174-200.
16. Tosi, A.; Calandri, N.; Sanzaro, M.; Acerbi, F., Low-noise, low-jitter, high detection efficiency InGaAs/InP single-photon avalanche diode. *IEEE Journal of selected topics in quantum electronics* **2014**, 20 (6), 192-197.

17. Namekata, N.; Sasamori, S.; Inoue, S., 800 MHz single-photon detection at 1550-nm using an InGaAs/InP avalanche photodiode operated with a sine wave gating. *Optics Express* **2006**, 14 (21), 10043-10049.
18. Yuan, Z.; Kardynal, B.; Sharpe, A.; Shields, A., High speed single photon detection in the near infrared. *Applied Physics Letters* **2007**, 91 (4), 041114.
19. Hayden, O.; Agarwal, R.; Lieber, C. M., Nanoscale avalanche photodiodes for highly sensitive and spatially resolved photon detection. *Nature materials* **2006**, 5 (5), 352.
20. Yang, C.; Barrelet, C. J.; Capasso, F.; Lieber, C. M., Single p-type/intrinsic/n-type silicon nanowires as nanoscale avalanche photodetectors. *Nano letters* **2006**, 6 (12), 2929-2934.
21. Reimer, M. E.; Van Kouwen, M. P.; Barkelid, M.; Hocevar, M.; Van Weert, M. H.; Algra, R. E.; Bakkers, E. P.; Björk, M. T.; Schmid, H.; Riel, H., Single photon emission and detection at the nanoscale utilizing semiconductor nanowires. *Journal of Nanophotonics* **2011**, 5 (1), 053502.
22. Yang, K.; Kwak, K.; Kim, S., Influence of the intrinsic length on p+-i-n+ Si nanowire avalanche photodetectors on flexible plastic substrates. *physica status solidi (c)* **2014**, 11 (2), 217-221.
23. Chuang, L. C.; Sedgwick, F. G.; Chen, R.; Ko, W. S.; Moewe, M.; Ng, K. W.; Tran, T.-T. D.; Chang-Hasnain, C., GaAs-based nanoneedle light emitting diode and avalanche photodiode monolithically integrated on a silicon substrate. *Nano letters* **2010**, 11 (2), 385-390.
24. Bulgarini, G.; Reimer, M. E.; Hocevar, M.; Bakkers, E. P.; Kouwenhoven, L. P.; Zwiller, V., Avalanche amplification of a single exciton in a semiconductor nanowire. *Nature Photonics* **2012**, 6 (7), 455.

25. Jain, V.; Heurlin, M.; Barrigon, E.; Bosco, L.; Nowzari, A.; Shroff, S.; Boix, V.; Karimi, M.; Jam, R. J.; Berg, A., InP/InAsP Nanowire-Based Spatially Separate Absorption and Multiplication Avalanche Photodetectors. *ACS Photonics* **2017**, 4 (11), 2693-2698.
26. Senanayake, P.; Hung, C.-H.; Farrell, A.; Ramirez, D. A.; Shapiro, J.; Li, C.-K.; Wu, Y.-R.; Hayat, M. M.; Huffaker, D. L., Thin 3D multiplication regions in plasmonically enhanced nanopillar avalanche detectors. *Nano letters* **2012**, 12 (12), 6448-6452.
27. Farrell, A. C.; Senanayake, P.; Hung, C.-H.; El-Howayek, G.; Rajagopal, A.; Currie, M.; Hayat, M. M.; Huffaker, D. L., Plasmonic field confinement for separate absorption-multiplication in InGaAs nanopillar avalanche photodiodes. *Scientific reports* **2015**, 5, 17580.
28. Guo, Y.-N.; Xu, H.-Y.; Auchterlonie, G. J.; Burgess, T.; Joyce, H. J.; Gao, Q.; Tan, H. H.; Jagadish, C.; Shu, H.-B.; Chen, X.-S., Phase separation induced by Au catalysts in ternary InGaAs nanowires. *Nano letters* **2013**, 13 (2), 643-650.
29. Jabeen, F.; Rubini, S.; Grillo, V.; Felisari, L.; Martelli, F., Room temperature luminescent InGaAs/GaAs core-shell nanowires. *Applied Physics Letters* **2008**, 93 (8), 083117.
30. Regolin, I.; Sudfeld, D.; Lüttjohann, S.; Khorenko, V.; Prost, W.; Kästner, J.; Dumpich, G.; Meier, C.; Lorke, A.; Tegude, F.-J., Growth and characterisation of GaAs/InGaAs/GaAs nanowhiskers on (111) GaAs. *Journal of crystal growth* **2007**, 298, 607-611.
31. Tatebayashi, J.; Kako, S.; Ho, J.; Ota, Y.; Iwamoto, S.; Arakawa, Y., Room-temperature lasing in a single nanowire with quantum dots. *Nature Photonics* **2015**, 9 (8), 501.
32. Yang, L.; Motohisa, J.; Takeda, J.; Tomioka, K.; Fukui, T., Size-dependent photoluminescence of hexagonal nanopillars with single In Ga As/ Ga As quantum wells

- fabricated by selective-area metal organic vapor phase epitaxy. *Applied physics letters* **2006**, 89 (20), 203110.
33. Shapiro, J.; Lin, A.; Wong, P.; Scofield, A.; Tu, C.; Senanayake, P.; Mariani, G.; Liang, B.; Huffaker, D., InGaAs heterostructure formation in catalyst-free GaAs nanopillars by selective-area metal-organic vapor phase epitaxy. *Applied Physics Letters* **2010**, 97 (24), 243102.
 34. Caneau, C.; Bhat, R.; Chang, C.; Kash, K.; Koza, M., Selective organometallic vapor phase epitaxy of Ga and In compounds: a comparison of TMIn and TEGa versus TMIn and TMGa. *Journal of crystal growth* **1993**, 132 (3-4), 364-370.
 35. Kim, H.; Ren, D.; Farrell, A. C.; Huffaker, D. L., Catalyst-free selective-area epitaxy of GaAs nanowires by metal-organic chemical vapor deposition using triethylgallium. *Nanotechnology* **2018**, 29 (8), 085601.
 36. Ren, D.; Farrell, A. C.; Huffaker, D. L., Axial InAs (Sb) inserts in selective-area InAsP nanowires on InP for optoelectronics beyond 2.5 μm . *Optical Materials Express* **2018**, 8 (4), 1075-1081.
 37. Zhang, J.; Itzler, M. A.; Zbinden, H.; Pan, J.-W., Advances in InGaAs/InP single-photon detector systems for quantum communication. *Light: Science & Applications* **2015**, 4, e286.
 38. Richardson, J. A.; Grant, L. A.; Webster, E. A.; Henderson, R. K. In *A 2 μm diameter, 9hz dark count, single photon avalanche diode in 130nm cmos technology*, 2010 Proceedings of the European Solid State Device Research Conference, 2010; pp 257-260
 39. Cova, S.; Ghioni, M.; Lacaita, A.; Samori, C.; Zappa, F., Avalanche photodiodes and quenching circuits for single-photon detection. *Applied optics* **1996**, 35 (12), 1956-1976.

40. Groves, C.; Ghin, R.; David, J.; Rees, G., Temperature dependence of impact ionization in GaAs. *IEEE Transactions on Electron Devices* **2003**, 50 (10), 2027-2031.
41. Donnelly, J. P.; Duerr, E. K.; McIntosh, K. A.; Dauler, E. A.; Oakley, D. C.; Groves, S. H.; Vineis, C. J.; Mahoney, L. J.; Molvar, K. M.; Hopman, P. I.; Jensen, K. E.; Smith, G. M.; Verghese, S.; Shaver, D. C., Design consideration for 1.06- μm InGaAsP-InP geiger-mode avalanche photodiodes. *IEEE Journal of Quantum Electronics* **2006** 42(8), 797-809.
42. Lunghi, T.; Barreiro, C.; Guinnard, O.; Houlmann, R.; Jiang, X.; Itzler, M. A.; Zbinden, H., Free-running single-photon detection based on a negative feedback InGaAs APD. *Journal of Modern Optics* **2012**, 59 (17), 1481-1488.
43. Senanayake, P.; Hung, C.-H.; Shapiro, J.; Lin, A.; Liang, B.; Williams, B. S.; Huffaker, D., Surface plasmon-enhanced nanopillar photodetectors. *Nano letters* **2011**, 11 (12), 5279-5283.
44. Ren, D.; Rong, Z.; Minh, C.; Farrell, A. C.; Meng, X.; Huffaker, D. L., Feasibility of room-temperature mid-wavelength infrared photodetectors using InAsSb nanostructured photoabsorbers. *Proceedings of SPIE* **2018**, 10531, 105310Y
45. Karimi, M.; Heurlin, M.; Limpert, S.; Jain, V.; Zeng, X.; Geijselaers, I.; Nowzari, A.; Fu, Y.; Samuelson, L.; Linke, H.; Borgström, M.; Pettersson, H., Intersubband quantum disc-in-nanowire photodetectors with normal-incidence response in the long-wavelength infrared. *Nano letters* **2018**, 18(1), 365-372.
46. Mariani, G.; Scofield, A. C.; Hung, C.-H.; Huffaker, D. L., GaAs nanopillar-array solar cells employing in situ surface passivation. *Nature communications* **2013**, 4:1497.

47. Farrell, A. C.; Senanayake, P.; Meng, X.; Hsieh, N. Y.; Huffaker, D. L., Diode characteristics approaching bulk limits in GaAs nanowire array photodetectors. *Nano letters* **2017**, 17 (4), 2420-2425.
48. Higuera-Rodriguez, A.; Romeira, B.; Birindelli, S.; Black, L.; Smalbrugge, E.; Van Veldhoven, P.; Kessels, W.; Smit, M.; Fiore, A., Ultralow surface recombination velocity in passivated InGaAs/InP nanopillars. *Nano letters* **2017**, 17 (4), 2627-2633.

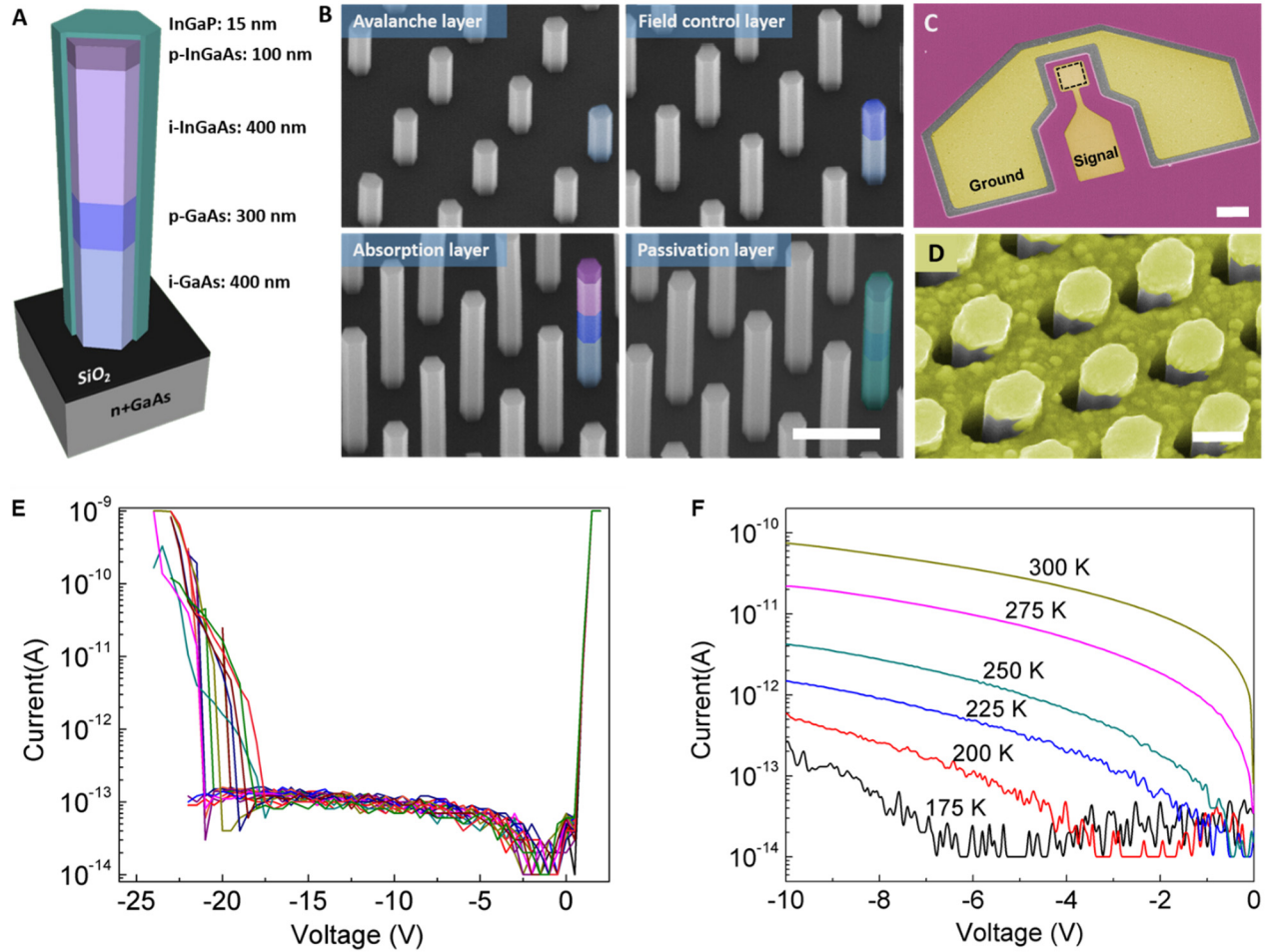


Figure 1. Design, fabrication, and dark current characteristics of nanowire SAM-APDs. (a) Schematic drawing of nanowire SAM-APD structure composed of InGaAs absorption layer, GaAs avalanche layer, and InGaP passivation shell. (b) SEM images of nanowire growth after each layer. Scale bar 500 nm. (c) False-color SEM of device after fabrication. Dashed box represents the position of nanowire arrays. Scale bar, 50 μ m. (d) Close-up false-color SEM of active area showing exposed nanowire tips. Scale bar, 200 nm. All SEM images are measured by tilting the sample by 30°. (e) Repeated DC voltage sweeps on a nanowire SAM-APD at 77 K. Although the breakdown voltage shifted randomly between -17 V and -22 V, there was no degradation of electrical characteristics after repeated measurements. (f) Temperature-dependent dark current showing that the leakage current is entirely below the system noise floor below 175 K.

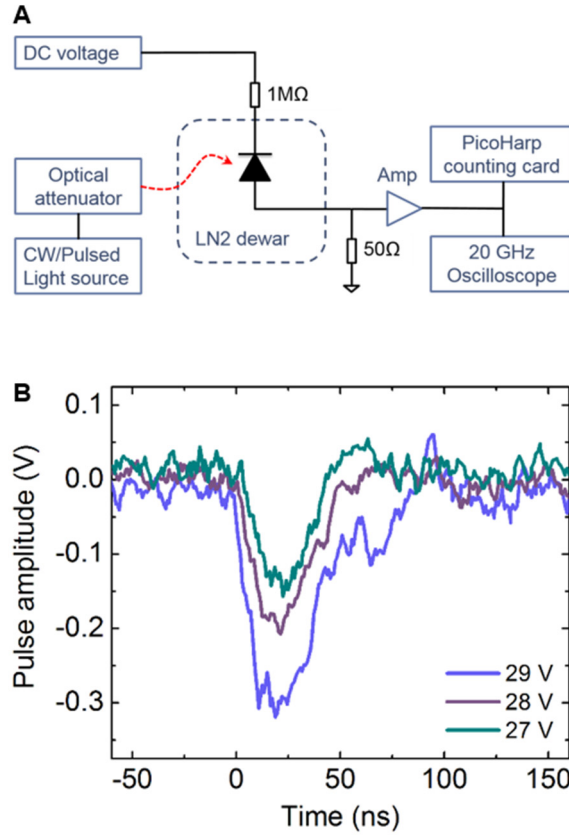


Figure 2. Photon counting setup and pulse measurements. (a) Configuration of the free-running mode measurement setup for dark counts and photon counts. Passive quenching is accomplished with a 1 MΩ resistor in series with the nanowire SAM-APD. (b) Pulse shape of dark carrier-initiated avalanche events for increasing DC bias.

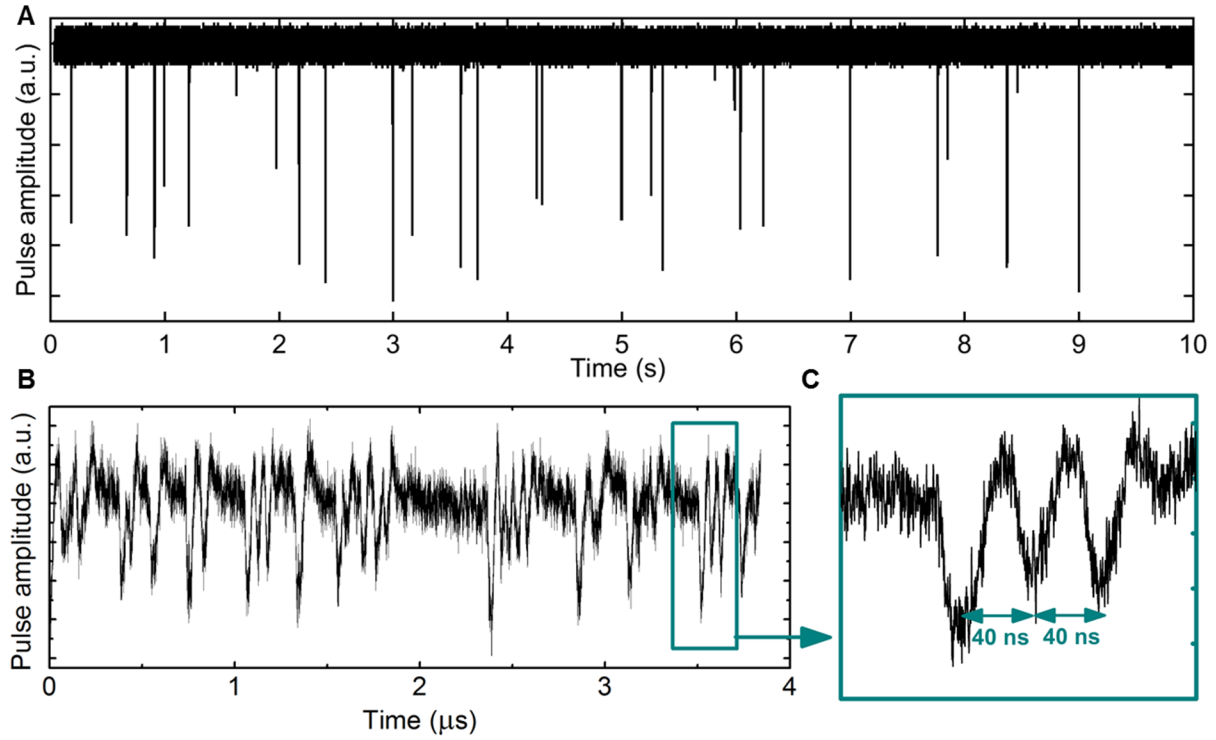


Figure 3. Temporal response of nanowire SAM-APDs in free-running mode. (a) Pulses under dark conditions arrive at a rate of 2.8 Hz. (b) Pulses under CW illumination arrives at a rate of 7.8 MHz. Note that the pulses occur much more frequently under illumination and thus the time scale is modified for clarity. (c) Close-up view of three consecutive pulses, with 40 ns time interval between pulses, indicating a maximum count rate of 25 MHz.

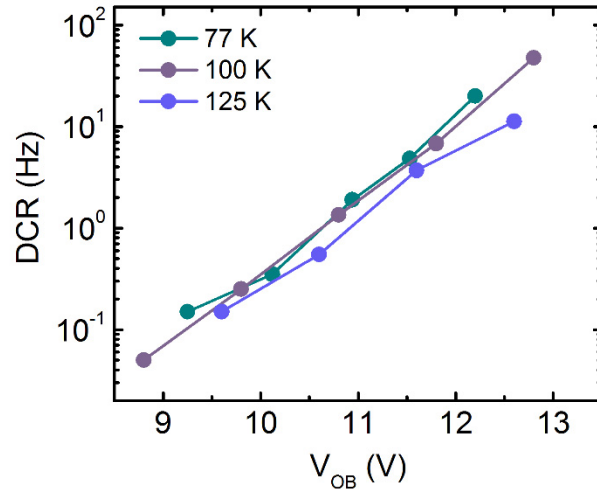


Figure 4. Dark count rate. The DCR was measured from 77 K to 125 K as a function of overbias, V_{OB} . At higher temperatures the average DCR fluctuated significantly and was therefore considered unstable and not included in this figure.

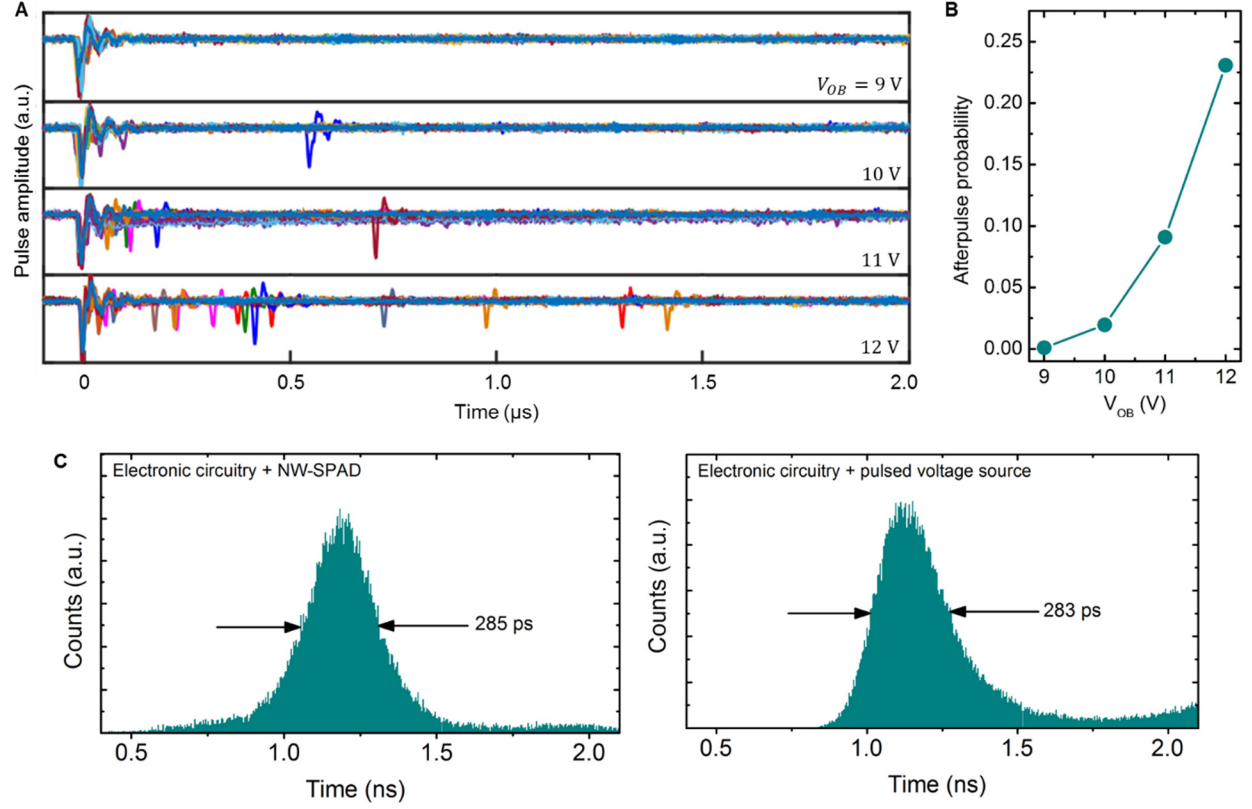


Figure 5. Afterpulsing and timing jitter. (a) Real-time sweeps spanning 2 μs at various applied V_{OB} . Afterpulsing begins to appear at V_{OB} of 10 V. (b) The maximum afterpulsing probability of 23 % occurs at V_{OB} of 12 V. (c) Experimental histograms obtained by measuring the timing distribution of a pulsed voltage source with a known timing jitter of 20 ps (top image), and the nanowire SAM-APDs with unknown timing jitter (bottom image). By comparing with the pulsed voltage source, timing jitter of nanowire SAM-APDs is deduced to be less than 113 ps.